RSC Advances

This is an *Accepted Manuscript*, which has been through the Royal Society of Chemistry peer review process and has been accepted for publication.

Accepted Manuscripts are published online shortly after acceptance, before technical editing, formatting and proof reading. Using this free service, authors can make their results available to the community, in citable form, before we publish the edited article. This *Accepted Manuscript* will be replaced by the edited, formatted and paginated article as soon as this is available.

You can find more information about *Accepted Manuscripts* in the **Information for Authors**.

Please note that technical editing may introduce minor changes to the text and/or graphics, which may alter content. The journal's standard **Terms & Conditions** and the **Ethical guidelines** still apply. In no event shall the Royal Society of Chemistry be held responsible for any errors or omissions in this *Accepted Manuscript* or any consequences arising from the use of any information it contains.

Journal Name

COMMUNICATION

Facile synthesis of Mn-doped hollow Fe_2O_3 nanospheres coated with polypyrrole as anode for high-performance lithium-ion batteries

Guangda Li,* Rumeng Han, Xiaoyun Xu and Manman Ren

Mn-doped Fe_2O_3/PPy hollow composite nanospheres were fabricated by a facile solvothermal method. Mn-Fe_2O_3/PPy electrode showed an improved electrochemical performance in terms of high rate capability and long cycling performance comparing with Fe_2O_3 without Mn doped and PPy coating. At current densities of 500 mA g^{-1} and 1000 mA g^{-1}, the Mn-Fe_2O_3/PPy exhibited an initial capacity of 1214.7 and 924.9 mAh g^{-1}, and the capacity was maintained at 795.7 and 643.6 mAh g^{-1} after 200 cycles.

1. Introduction

With increasing demand for next generation portable electronic devices and electric vehicles, the development of lithium-ion batteries (LIBs) with high capacity, excellent cycling performance, and superior rate capability is becoming a crucial question gradually.[1-3] Among various promising materials, transition metal oxides, such as SnO_2, Fe_2O_3, TiO_2 and Co_3O_4, have been widely studied as anode materials for LIBs.[4-9] Among them, Fe_2O_3 have been attracting more and more attention owing to its high theoretical capacity (1074 mAh g^{-1}), low cost, high safety and environmental friendliness.[10-12] However, Fe_2O_3 used as electrode for LIBs usually suffers from poor cycling performance and bad rate capability caused by its low electrical conductivity and large volume change ($>$200%) during the insertion/extraction and pulverization process.[13,14] To overcome these drawbacks, extensive researches have been focused on alleviating various nanostructures and/or improving the electronic conductivity by using graphite coating.

One effective way is to fabricate hollow nanostructure Fe_2O_3.[15-19] Hollow nanostructures with high surface area and high specific capacity have attracted much attention because hollow anode materials can supply more Li^+ ion sites, alleviate the volume expansion and shorten the diffusion length for Li^+

ion intercalation. Lou et al. have demonstrated that hollow structure can improve contact between electrolyte and active materials, superior electrochemical kinetics and remarkable structural stability in their previous works. Although some nanostructure anodes showed relative high capacities, the electronic conductivity of the Fe_2O_3 materials are not improved obviously, which could result in poor cycling performance and rate capability during long discharge/charge cycles.

Furthermore, the surface coating of inorganic nanoparticles by conducting polymers have been extensively studied and applications.[20,21] Polypyrrole (PPy) is a conductivity polymer with ion-penetrating ability, excellent mechanical properties and high electrochemical performance. Coating of PPy has also been successfully applied in the property enhancement of LIBs, such as MnO_2/PPy, SnO_2/PPy and Fe_2O_3/PPy.[22-24]

Recently, a number of studies have shown that the electronic conductivity and cycling performance of metal oxide materials (NiO, SnO_2, TiO_2, ZnO, Fe_2O_3 and $ZnFe_2O_4$) can be significantly enhanced by doping other elements (Co, Cu, Ni, Fe, Mn, and Zn).[12,25-32] Doping other metal ions in crystal structure can cause a change in the unite cell volume, thus leading to Li^+ diffusion easier. Furthermore, doping other metal ions may act as a buffer to alleviate the stress which caused by the volume change during discharge/charge process. For example, Liu et al. reported Mn-doped Fe_2O_3 hollow porous prisms exhibit an improved electrochemical performance compared with pristine Fe_2O_3.[17] Thi et al. also introduced Co-doped NiO by a facile solvothermal method. It was found that the conductivity of NiO is largely improve through Co^{2+} doping and the Co-doped NiO anode revealed greatly enhanced rate capability and excellent cycling performance.[12]

In this work, we proposed that hollow Mn-doped Fe_2O_3 (Mn-Fe_2O_3) nanospheres to improving the performance of LIBs. First, the similar ion radii of Mn^{2+} (0.067 nm) and Fe^{3+} (0.055 nm) would make it possible to doped Fe_2O_3 by Mn without causing much lattice strain. Second, the radius of Mn^{2+} is larger than Fe^{3+}, so the replacement of Fe^{3+} by Mn^{2+} in crystal

Key Laboratory of Processing and Testing Technology of Glass & Functional Ceramics of Shandong Province, School of Material Science and Engineering, Qilu University of Technology, Jinan, 250353, China. E-mail: ligd@qlu.edu.cn

structure can cause an increase in the unite cell volume, thus making Li^+ ion diffusion easier. This also means the intrinsic conductivity of $Mn-Fe_2O_3$ can be improved.[31] Furthermore, in order to further improve the conductivity and stability of $Mn-Fe_2O_3$, conductive and soft polymers of polypyrrole (PPy) are constructed uniform hybrid structure of $Mn-Fe_2O_3/PPy$. In this way, the hybrid structure of $Mn-Fe_2O_3/PPy$, in which $Mn-Fe_2O_3$ nanospheres are evenly embedded in the PPy matrix, is believed as a significantly innovation for developing novel electrode materials with improved electrochemical performance.

2. Experimental Section

2.1 Preparation of Mn-doped Fe_2O_3

In a typical experimental procedure, 2 mmol $FeCl_3·6H_2O$ and 4 mmol $Mn(CH_3COO)_2·4H_2O$ were dissolved in 30 ml ethylene glycol under vigorous stirring. Then, 0.5 g NH_4AC was added into the above solution. The mixture solution was stirred for 30 min to obtain a homogeneous solution and transferred into a 40 ml Teflon-lined stainless-steel autoclave. The autoclave was sealed and heated at 180 ℃ for 30 h in an electronic oven. After cooling naturally, the precipitates were collected and washed with absolute ethanol and deionized water for several times, and dried at 80 ℃ for 5 h in vacuum oven. This precursor was heated in a furnace at 500 ℃ for 3 h in atmosphere. At last, the hollow Mn-doped Fe_2O_3 nanopspheres could be obtained. For the synthesis of hollow Fe_2O_3 without Mn doped, the process was carried out in a similar way to prepared Mn-doped Fe_2O_3 except no $Mn(CH_3COO)_2·4H_2O$ added in system.

2.2 Preparation of $Mn-Fe_2O_3/PPy$

The as-prepared $Mn-Fe_2O_3$ nanospheres (20 mg) were dispersed in deionized water (100 ml) by ultrasonication for 30 min. Then the pyrrole (50 μl) was added in the solution. After the solution was stirred for 1 h, $(NH_4)_2S_2O_8$ (0.1 M, 10 ml) solution was added in droplets and the stirring continued for 4 h. The resulting $Mn-Fe_2O_3/PPy$ was collected by filtration and washed with deionized water and ethanol.

2.3 Material characterization

The X-ray power diffraction (XRD) analysis was performed on a Bruker D8 advanced X-ray diffractometer equipped with graphite-monochromatized CuKα radiation (λ = 1.5418 Å). The morphologies of the products were observed through scanning electron microscopy (SEM) and transmission electron microscope (TEM) measurements, which were carried out on a JEOL JSM-7600F field emission instrument and a JEM 1011 TEM, respectively. High-resolution transmission electron microscope (HRTEM) images were carried out on a JEOL 2100 transmission electron microscope with an accelerating voltage of 200 KV. The chemical composition of the samples was analyzed by X-ray photoelectron instruments (XPS, VGESCALABMK X-ray spectrometer). The ICP was carried out on Optima 2000DV. Brunauer-Emmett-Teller (BET) test was performed on surface area and porosity analyzer (Micromeritics, ASAP 2020).

2.4 Electrochemical measurements

The working electrodes were prepared by pasting mixed slurry that consisted of 70 wt% active materials ($Mn-Fe_2O_3/PPy$), 10 wt% sodium carboxy methyl cellulose (CMC), and 20 wt% carbon black onto a copper foil. The fabricated working electrodes dried in vacuum oven at 100 ℃ for 24 h. Celgard 2400 microporous polypropylene membrane was used as separator. The electrolyte consisted of a solution of 1 M $LiPF_6$ in an ethylene carbonate/dimethyl carbonate/diethyl carbonate (EC/DMC/DEC, 1:1:1 w/w). Lithium foils were used as counter electrodes. The batteries were assembled in an argon-filled glove box and cycled at different current density between voltage limits of 0.01 and 3.0 V. Cyclic voltametry (CV) profiles (0.01-3.0 V, 0.1 mV S^{-1}) were carried out on an electrochemical workstation (CHI 760E, China). The discharge/charge tests of the samples were carried out on a Land battery test system (CT2001A).

3. Results and discussion
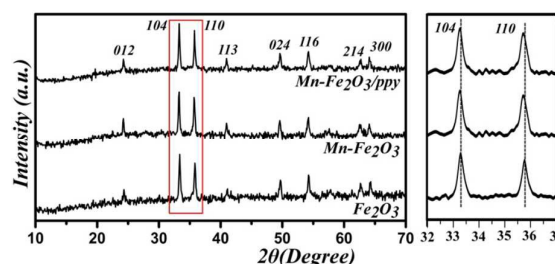
Fig. 1 XRD pattern of Fe_2O_3, $Mn-Fe_2O_3$ and $Mn-Fe_2O_3/PPy$ samples, and the diffraction peak range from 32 to 37 degree for each pattern was magnified and indexed to (104) and (110) reflection.

Fig. 1 shows the XRD patterns of Fe_2O_3, $Mn-Fe_2O_3$ and $Mn-Fe_2O_3/PPy$, respectively. XRD pattern of both the undoped and Mn-doped samples could be indexed by the standard reflection data of α-Fe_2O_3 (JCPDS no. 33-0664). Therein, the magnified (104) and (110) face reflection peaks of the Mn-doped Fe_2O_3 indicate that there is a slight shift to the left. This suggests that element Mn is highly dispersed in the matrix of crystalline α-Fe_2O_3, and this phenomenon also coincides with Bragg equation. The Fe/Mn element ratio is determined by the ICP method, giving a chemical formula of $Fe_{1.8}Mn_{0.2}O_3$ for the obtained Mn-doped Fe_2O_3 samples.
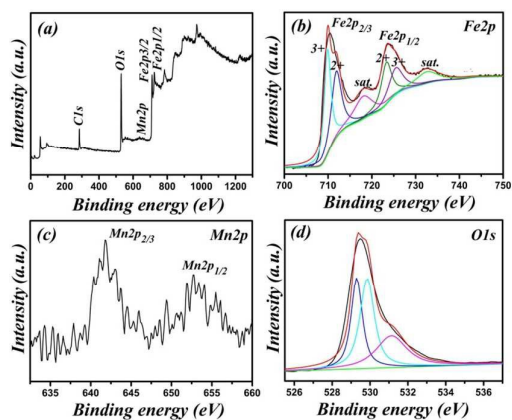
Fig. 2 XPS spectra of the hollow Mn-Fe$_2$O$_3$ nanospheres: (a) Survey spectrum; (b) Fe$_{2p}$; (c) Mn$_{2p}$; (d) O$_{1s}$.

XPS spectra are presented in Fig. 2. The survey spectrum (Fig. 2a) shows that the presence of Fe, Mn, O and C from the reference. The spectrum of Fe$_{2p}$ (Fig. 2b) shows two obviously peaks of Fe$_{2p3/2}$ at 710.1 eV and Fe$_{2p1/2}$ at 724.4 eV, and the separation of the 2p doublet is ~14.0 eV.[33] Furthermore, there are two shake-up satellites at binding energies of 717.6 and 732.6 eV, which are also clearly observed.[20] All of these features can be ascribed to Fe$_2$O$_3$. By using a Gaussian fitting method, the Fe$_{2p}$ spectrum is best fitted to two spin-orbit doublets characteristic of Fe^{3+} and Fe^{2+}, which suggests that the presence of slight Fe^{2+}.[34,35] This phenomenon may be caused by defects of the Fe$_2$O$_3$ crystal surface. The peaks at 641.8 and 652.7 eV can be attributed to Mn$_{2p3/2}$ and Mn$_{2p1/2}$, respectively (Fig. 2c).[36] The high-resolution spectrum of O$_{1s}$ (Fig. 2d) can be fitted into three oxygen contributions. The peak at 532.2 eV corresponds to O^{2-} in Fe$_2$O$_3$. The peak at 529.6 eV is attributed to defects and contaminates a number of surface species including hydroxyls, chemisorbed oxygen and water on the surface of Fe$_2$O$_3$.[12] The peak at 531.1 eV can be assigned to the coordination of oxygen in Mn-O. Based on the results of XPS, it could be inferred that Mn ions were successfully incorporated into Fe$_2$O$_3$.
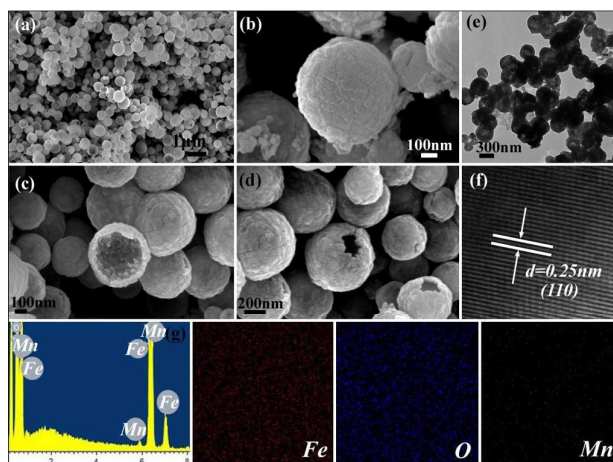
Fig. 3 (a-d) Typical SEM images of the Mn-Fe$_2$O$_3$ hollow nanospheres; (e,f) TEM and HRTEM images of the Mn-Fe$_2$O$_3$; (g) EDS and element mapping of the Mn-Fe$_2$O$_3$.

Fig. 3 shows the SEM and TEM images of the hollow Mn-Fe$_2$O$_3$ nanospheres in order to observing the morphologies and nanostructures. From Fig. 3a-d, it is indicated that the synthesized Mn-Fe$_2$O$_3$ display a smooth surface with a highly uniform morphology with an average size of about 300~600 nm. The high resolution SEM image as shown in Fig. 3c and d clearly presents the open tip, implying a hollow structure. Fig. 3e shows a typical TEM image of Mn-Fe$_2$O$_3$, and the obvious contrast between the centers and shells of the spherical particles demonstrates a hollow structure obtained. The thickness of the shell is about 50 nm. HRTEM image (Fig. 3f) clearly shows distinct lattice fringes with d spacing of 0.25 nm, corresponding to the (110) lattice planes of Fe$_2$O$_3$. The EDS (Fig. 3f) reveals the co-existence of Fe, O and Mn in the structure, further indicating the successful synthesis of Mn-Fe$_2$O$_3$. The mapping images display the uniform distribution of all elements (Fe, O and Mn), indicating Mn are highly dispersed in the Fe$_2$O$_3$ structure.
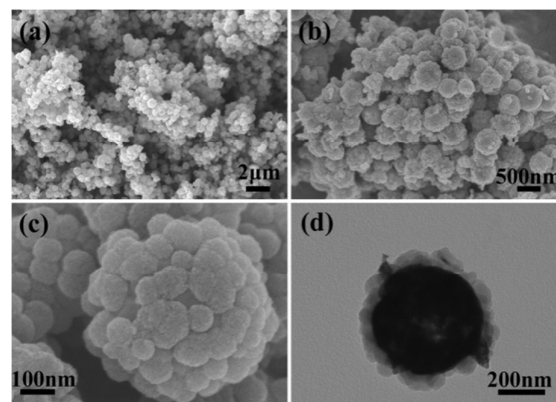
Fig. 4 (a-c) Typical SEM images of the Mn-Fe$_2$O$_3$/PPy; (d) TEM image of the Mn-Fe$_2$O$_3$/PPy.

Fig. 4a and b shows typical SEM and TEM image of Mn-Fe$_2$O$_3$/PPy. These composite nanospheres exhibited rough outer surface comparing with Mn-Fe$_2$O$_3$, which is believed to be the PPy layers coated on the surface of Fe$_2$O$_3$. The clearly PPy layers on the surface of Fe$_2$O$_3$ can be clearly observed from Fig. 4c and d. As shown in Fig. 4c, the PPy nanoparticles compactly growth on the surface of Fe$_2$O$_3$ formed PPy layers. The size of PPy particles is about 30-50 nm. From Fig. 4d, it can be seen that the thickness of PPy layers is about 50 nm. The conductivity polymer of PPy growth on the surface of Mn-Fe$_2$O$_3$ can significantly improve the electronic conductivity and alleviate the volume change during the discharge/charge cycles. These favorable factors can result in superior cycling performance and rate capability.
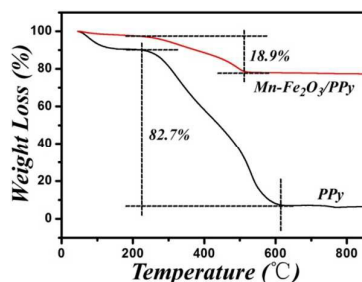
Fig. 5 TGA curves of the Mn-Fe$_2$O$_3$/PPy and pristine PPy under N$_2$ atmosphere.

Typical TGA curves of the Mn-Fe$_2$O$_3$/PPy and PPy under N$_2$ atmosphere are shown in Fig. 5. As shown in the TGA curve of Mn-Fe$_2$O$_3$/PPy, the first weight loss, occurring below 220 ℃, is attributed to a little loss of water absorbed on the surface of samples.[37] This weigh loss temperature is also clearly observed from PPy curve. From the 220 to 500 ℃, the observed weight loss is due to the combustion of PPy.[38] According to this TGA curve, the weight percentage of PPy in composites is about 18.7%.
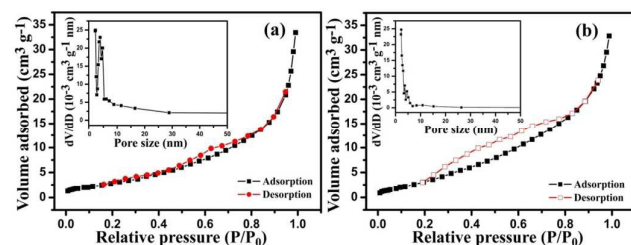
Fig. 6 N$_2$ adsorption/desorption isotherms and the corresponding pore size distribution (inset) of (a) Mn-Fe$_2$O$_3$ and (b) Mn-Fe$_2$O$_3$/PPy.

Fig. 6 shows the specific surface areas for Mn-Fe$_2$O$_3$ and Mn-Fe$_2$O$_3$/PPy, which are 12.22 and 14.52 m^2 g^{-1}, respectively. The insets in Fig. 6 are the corresponding pore size distributions estimated using the BJH method, giving pore diameters with values of 9.87 and 7.09 nm for Mn-Fe$_2$O$_3$ and Mn-Fe$_2$O$_3$/PPy. PPy coating on the surface of Mn-Fe$_2$O$_3$ resulted in the specific surface area increasing, indicating more Li$^+$ insertion/extraction sites during cycles.
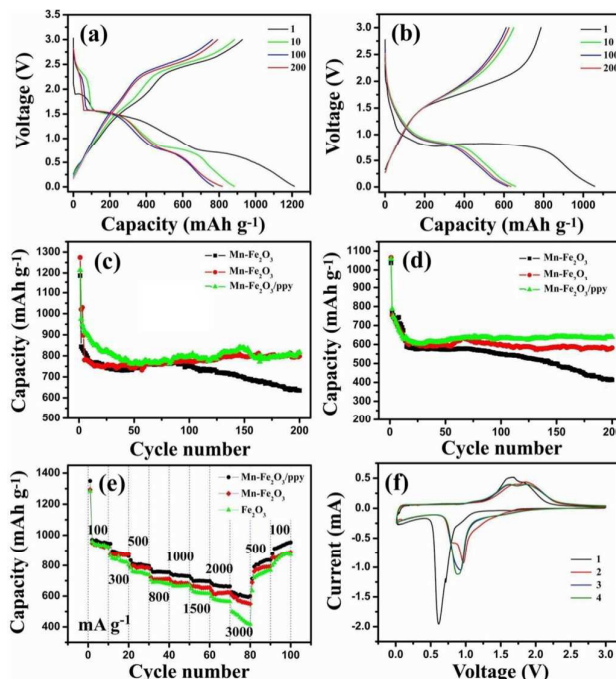
Fig. 7 The discharge/charge curves of the Mn-Fe$_2$O$_3$/PPy at current density of (a) 500 and (b) 1000 mA g^{-1}. Cycling performance of the Fe$_2$O$_3$, Mn-Fe$_2$O$_3$ and Mn-Fe$_2$O$_3$/PPy electrode at 500 mA g^{-1} (c) and 1000 mA g^{-1} (d). (e) Rate capability of the Fe$_2$O$_3$, Mn-Fe$_2$O$_3$ and Mn-Fe$_2$O$_3$/PPy electrode at different current densities. (f) The first four consecutive CV curves of the Mn-Fe$_2$O$_3$/PPy electrode in the voltage range of 0.01-3.0 V at a scan rate of 0.1 mV s^{-1}.

The discharge/charge curves of the Mn-Fe$_2$O$_3$/PPy nanospheres for the different cycles at current densities of 500 and 1000 mA g^{-1} are shown in Fig. 7a and b. The initial discharge and charge capacities of Mn-Fe$_2$O$_3$/PPy are 1214.7 and 924.9 mAh g^{-1}, corresponding to 76.1% of the first Coulombic efficiency at current density of 500 mA g^{-1}. The irreversible capacity loss in the first discharge/charge process can be attributed to the decomposition of electrolyte and the formation of SEI on the surface of electrode, which is commonly observed in metal oxide anode materials. At a current density of 1000 mA g^{-1}, the Mn-Fe$_2$O$_3$/PPy exhibits an initial discharge capacity of 1061.8 mAh g^{-1} and a charge capacity of 787.0 mAh g^{-1} leading to a coulombic efficiency of 74.1%.

The cycling performance of Fe$_2$O$_3$, Mn-Fe$_2$O$_3$ and Mn-Fe$_2$O$_3$/PPy are presented in Fig. 7c and d. A high capacity as high as 801.6 mAh g^{-1} is sill maintained even after 200 cycles at 500 mAh g^{-1} of Mn-Fe$_2$O$_3$/PPy, which suggest an excellent cycling stability. For the purpose of comparison, the electrochemical properties of pristine Fe$_2$O$_3$ and Mn-Fe$_2$O$_3$ nanospheres are also examined. The Mn-Fe$_2$O$_3$ shows an initial discharge of 1272.1 mAh g^{-1}, fading to 795.7 mAh g^{-1} after 200 cycles at 500 mAh g^{-1}. Pristine Fe$_2$O$_3$ nanospheres exhibit a relatively low reversible capacity of approximately 559.4 mAh g^{-1} with a poor cycling stability. These results demonstrate that Mn-Fe$_2$O$_3$ and Mn-Fe$_2$O$_3$/PPy have no large difference at relatively low current density, such as 500 mAh g^{-1}. When the current density increased to 1000 mA g^{-1}, Mn-Fe$_2$O$_3$/PPy still

exhibited an excellent capacity of 643.6 mAh g^{-1} after 200 cycles. However, the Mn-Fe$_2$O$_3$ displayed 579.3 mAh g^{-1} at 1000 mA g^{-1} after 200 cycles, which is ~10% lower than that of Mn-Fe$_2$O$_3$/PPy.

Excellent performance of Mn-Fe$_2$O$_3$/PPy is obvious shown at relatively high current density comparing with Mn-Fe$_2$O$_3$ and pristine Fe$_2$O$_3$. The rate capabilities of Fe$_2$O$_3$, Mn-Fe$_2$O$_3$ and Mn-Fe$_2$O$_3$/PPy are further investigated at various current densities ranging from 100 to 3000 mAh g^{-1}. For the Mn-Fe$_2$O$_3$/PPy, a high average capacity of 953.3 mAh g^{-1} is achieved at 100 mA g^{-1}. The capacity decreases slightly with the stepwise increase of current density. Even at high density of 3000 mA g^{-1}, a capacity of 595.4 mAh g^{-1} can be still retained. Remarkably, a stable capacity of 937.4 mAh g^{-1} can be resumed when the current density is went back to 100 mA g^{-1}, which remains 98% of the initial capacity before the high rate discharge/charge test. Such an excellent electrochemical performance in terms of cycling performance and rate capability is superior to pristine Fe$_2$O$_3$ and Mn-Fe$_2$O$_3$ as anode for LIBs.

As shown in Fig. 7e, pristine Fe$_2$O$_3$ shows a rapidly capacity fading, especially at high current density. The Mn-Fe$_2$O$_3$ and Mn-Fe$_2$O$_3$/PPy electrode shows a similar trend during the rate capacity test but the capacity lower than that of Mn-Fe$_2$O$_3$/PPy at high rate. Furthermore, the capacity of Mn-Fe$_2$O$_3$ decayed obviously at high current density. This demonstrated that the conducting polymer, PPy, which coated on the surface of Mn-Fe$_2$O$_3$, is beneficial to the stability of the metal oxide structure during discharge/charge cycles.

Fig. 7f shows the first four CV curves of the Mn-Fe$_2$O$_3$/PPy electrode in the voltage range of 0.01-3.0 V at a scan rate of 0.1 mV s^{-1}. In the first cycles, a sharp reduction peak located at 0.62 V can be ascribed to Li insertion into Fe$_2$O$_3$ and formation of Li$_2$O.[16] In next cycles, the reduction peak at 0.62 V moved to 0.87 V. It has been proposed that the Li ions insertion in Fe$_2$O$_3$ mainly based on a multiple steps, the phase transformation from Li$_x$Fe$_2$O$_3$ to Li$_2$Fe$_2$O$_3$, the complete reduction of Li$_2$Fe$_2$O$_3$ to Fe^0 and Li$_2$O.[16] In the anodic scan, two broad oxidation peaks are observed at 1.61 V and 1.87 V, which correspond to the oxidation of Fe^0 to Fe^{2+} and Fe^{2+} to Fe^{3+}, respectively.[15] From the second cycle, CV curves exhibit little change, including a good reversibility of the electrochemical reaction (Fe$_2$O$_3$ + 6Li $\rightleftharpoons$ 2Fe + 3Li$_2$O).[39]

The high reversible capacity, excellent cycling performance and outstanding rate capability can be attributed to the unique structure of Mn-Fe$_2$O$_3$/PPy. First, hollow nanosphere of Mn-Fe$_2$O$_3$ are beneficial for the electrolyte penetration, Li$^+$ ion diffusion and alleviate the volume change. Second, doping other element in metal oxide may be cause an increase in the unite cell volume, thus making Li$^+$ ion diffusion easier and crystal more stable. Third, the PPy coating sever three main purposes: (1) The PPy layers serve as the structural stabilizer, which buffer the large volume expansion, inhibit the aggregation and prevent the pulverization of Mn-Fe$_2$O$_3$ during the cycles. (2) PPy acts as a conducting polymer coating on the surface of Mn-Fe$_2$O$_3$, leading to enhance the conducting of Mn-Fe$_2$O$_3$. (3) The PPy layers serve as the interfacial stabilizer,

preventing the exposure of Mn-Fe$_2$O$_3$ nanospheres to the electrolyte, and thus forming a stable electrode-electrolyte interphase.

4. Conclusions

In summary, Mn-Fe$_2$O$_3$/PPy hollow nanospheres have been synthesized by a facile template-free method. When used as anode materials for LIBs, the Mn-Fe$_2$O$_3$/PPy exhibit excellent electrochemical performance. The great improvement performance can be attributed to the Mn doped, PPy coating and hollow structure. Mn-Fe$_2$O$_3$/PPy electrode shows high reversible capacity of 795.7 mAh g^{-1} after 200 cycles at a current density of 500 mA g^{-1}. Even at high rate of 1000 mA g^{-1}, this anode also exhibit 643.6 mAh g^{-1} after 200 cycles. The excellent performances of Mn-Fe$_2$O$_3$/PPy enable them to be a new candidate for next generation of energy storage and conversion devices.

Acknowledgements

References

1 J. M. Tarascon and M. Armand, *Nature*, 2001, **414**, 359.
2 L. Yu, H. B. Wu, G. Q. Zhang and X. W. Lou, *Energy Environ. Sci.*, 2013, **6**, 2664.
3 P. G. Bruce, B. Scrosati and J. M. Trascon, *Angew. Chem. Int. Ed.*, 2008, **47**, 293.
4 D. F. Sun, J. T. Chen, J. Yang and X. B. Yan, *CrystEngComm*, 2014, **16**, 10476.
5 B. C. Sekhar and N. Kalaiselvi, *CrystEngComm*, 2015, **17**, 5038.
6 P. Wang, M. X. Gao, H. G. Pan, J. L. Zhang, C. Liang, J. H. Wang, P. Zhou and Y. F. Liu, *J. Power Source*, 2013, **239**, 466.
7 X. Q. Han, X. Han, L. Q. Sun, Q. Q. Liu, W. Xu, L. Li, P. Wang and C. Wang, *CrystEngComm*, 2015, **17**, 1754.
8 N. Yan, L. Hu, Y. Li, Y. Wang, H. Zhong, X. Y. Hu, X. K. Kong and Q. W. Chen, *J. Phys. Chem. C*, 2012, **116**, 7227.
9 J. M. Jeong, B. G. Choi, S. C. Lee, K. G. Lee, S. J. Chang, Y. K. Han, Y. B. Lee, H. U. Lee, S. Kwon, G. Lee, C. S. Lee and Y. S. Huh, *Adv. Mater.*, 2013, **25**, 6250.
10 Z. G. Wu, Y. J. Zhong, J. Liu, J. H. Wu, X. D. Guo, B. H. Zhong and Z. Y. Zhang, *J. Mater. Chem. A*, 2015, **3**, 10092.
11 T. V. Thi, A. K. Rai, J. Gim and J. Kim, *J. Power Sources*, 2015, **292**, 23.
12 H. W. Zhang, X. R. Sun, X. D. Huang and L. Zhou, *Nanoscale*, 2015, **7**, 3270.
13 R. C. Jin, L. Yang, G. H. Li and G. Chen, *New J. Chem.*, 2014, **38**, 5840.
14 M. Y. Son, Y. J. Hong, J. K. Lee and Y. C. Kang, *Nanoscale*, 2013, **5**, 11592.
15 H. Xiao, Y. Xia, W. K. Zhang, H. Huang, Y. P. Gan and X. Y. Tao, *J. Mater. Chem. A*, 2013, **1**, 2307.
16 Y. H. Xu, G. Q. Jian, Y. H. Liu, Y. J. Zhu, M. R. Zachariah and C. S. Wang, *Nano Energy*, 2014, **3**, 26.
17 H. Liu and G. X. Wang, *J. Mater. Chem. A*, 2014, **2**, 9955.

18 J. S. Cho, Y. J. Hong, J. H. Lee and Y. C. Kang, *Nanoscale*, 2015, **7**, 8361.
19 Y. F. Liu, J. M. Xu and X. Y. Qin, *J. Mater. Chem. A*, 2015, **3**, 9682.
20 C. Gao and G. M. Chen, *Compos. Sci. Technol.*, 2016, **124**, 52.
21 K. L. Xu, G. M. Chen and D. Qiu, *J. Mater. Chem. A*, 2013, **1**, 12395.
22 M. Wang, Q. X. Yang, T. D. Zhang, B. K. Zhu and G. D. Li, *RSC Adv.*, 2016, **6**, 19952.
23 R. Q. Liu, Y. J. Liu, Q. Kang, A. Casimir, H. G. Zhang, N. Li, Z. D. Huang, Y. Li, X. J. Lin, X. M. Feng, Y. W. Ma and G. Wu, *RSC Adv.*, 2016, **6**, 9402.
24 J. L. Liu, W. Zhou, L. F. Lai, H. P. Yang, S. H. Lim, Y. D. Zhen, T. Yu, Z. X. Shen and J. Y. Lin, *Nano Energy*, 2013, **2**, 726.
25 G. D. Li, X. Y. Xu, R. M. Han and J, Y. Ma, *CrystEngComm*, 2016, **18**, 2949.
26 J. Y. Ma, L. W. Yin and T. R. Ge, *CrystEngComm*, 2015, **17**, 9336.
27 N. Wan, T. T. Zhao, S. W. Sun, Q. Wu and Y. Bai, *Electrochim. Acta*, 2014, **143**, 257.
28 Y. Ma, C. L. Fang, B. Ding, G. Ji and J. Y. Lee, *Adv. Mater.*, 2013, **25**, 4646.
29 W. Zhang, W. D. Zhou, J. H. Wright, Y. N. Kim, D. W. Liu and X. C. Xiao, *ACS Appl. Mater. Interfaces*, 2014, **6**, 7292.
30 Z. Ali, S. N. Cha, J. I. Sohn, I. Shakir, C. Yan, J. M. Kim and D. J. Kang, J. *Mater. Chem.*, 2012, **22**, 17625.
31 G. X. Lu, S. Qiu, J. R. Liu, X. Z. Wang, C. Z. He and Y. J. Bai, *Electrochim. Acta*, 2014, **117**, 230.
32 Y. X. Yang, W. W. Xu, R. S. Guo, L. Liu, S. S. Wang, D. Xie and Y. Z. Wan, *J. Power Sources*, 2014, **269**, 15.
33 I. Uhlig, R. Szargan, H. W. Nesbitt and K. Laajalehto, *Appl. Sur. Sci.*, 2001, **179**, 222.
34 L. R. Hou, L. Lian, L. H. Zhang, G. Pang, C. Z. Yuan and X. G. Zhang, *Adv. Funct. Mater.*, 2015, **25**, 238.
35 Y. C. Dong, Y. Xia, Y. S. Chui, C. W. Cao and J. A. Zapien, *J. Power Sources*, 2015, **275**, 769.
36 G. D. Li, L. Q. Xu, Y. J. Zhai and Y. P. Hou, *J. Mater. Chem. A*, 2015, **3**, 14298.
37 J. Ge, J. J. Shi and L. J. Chen, *Carbon*, 2009, **47**, 1192.
38 M. Wang, Q. X. Yang, T. D. Zhang, B. K. Zhu and G. D. Li, *RSC Adv.*, 2016, **6**, 19952.
39 Z. G. Wu, Y. J. Zhong, J. Liu, J. H. Wu, X. D. Guo, B. H. Zhong and Z. Y. Zhang, *J. Mater. Chem. A*, 2015, **3**, 10092.

Hollow Mn-doped Fe_2O_3/PPy nanospheres have been fabricated, which exhibited excellent electrochemical performance as an anode material for lithium-ion batteries.